Roughness Related to Cooling Performance of Channels Made Through Additive Manufacturing

Alexander J. Wildgoose[1]
Department of Mechanical Engineering,
Pennsylvania State University,
State College, PA 16801
e-mail: ajw324@0psu.edu

Karen A. Thole
Department of Mechanical Engineering,
Pennsylvania State University,
State College, PA 16801
e-mail: kthole@psu.edu

Erika Tuneskog
Siemens Energy AB,
Finspång 61231, Sweden
e-mails: erika.tuneskog@siemens-energy.com;
erika.tuneskog@chalmers.se

Lieke Wang
Siemens Energy Inc.,
Orlando, FL 32817
e-mail: lieke.wang@siemens-energy.com

The complex surface morphology and multiscale surface features inherent in additively manufactured (AM) components contribute to the overall flow characteristics and heat transfer of cooling passages. As the AM process and cooling data in the literature continue to evolve, so does the need for more accurate heat transfer and pressure loss correlations for AM cooling schemes. This study improves the predictability of pressure loss and heat transfer for AM cooling passages by fabricating a range of coupons and investigating samples in the literature. Twenty-seven test coupons were manufactured using direct metal laser sintering in an assortment of build directions and build locations that produced a variety of surface morphologies. Nondestructive evaluation, computed tomography scanning, was used to quantify the surface morphology as well as capture the as-built geometric dimensions of the cooling schemes. The friction factor and bulk Nusselt number of the coupons were measured using an experimental rig. Pressure loss and heat transfer correlations in the literature were compared with the experimental results from the current coupons and datasets from the literature. Arithmetic mean roughness correlations in the literature struggled to predict the cooling performance of AM channels since the bulk roughness statistic did not capture the overall form of the surface morphology. A combination of root mean square roughness and skewness of the roughness was able to best predict pressure loss and heat transfer for the present samples and those in the literature while being independent of build location, build direction, material, machine, and laser parameters. The maximum absolute error was 25% and the average absolute error was 12% for the friction factor correlation. The maximum absolute error was 39% and the average absolute error was 8% for the Nusselt Number correlation. [DOI: 10.1115/1.4064310]

Keywords: heat transfer, friction factor, roughness, additive manufacturing

Introduction

The metal additive manufacturing (AM) process is a key technology that enables quicker development of complex cooling designs, such as those seen in gas turbines, compared to subtractive or casting fabrication methods. A reduction in part assemblies and overall component weight can also be achieved due to the added design freedom offered through AM relative to traditional fabrication methods. A key characteristic inherent in the AM process, specifically direct metal laser sintering (DMLS), is the as-built surface roughness. Several studies [1,2] have shown that surface roughness is one of the main drivers that influence the turbulent mixing and resulting heat transfer enhancement of AM cooling schemes compared to traditionally fabricated designs. The magnitude and size of the roughness features are particularly important in submillimeter internal channels since these features directly influence the overall convective heat transfer.

The rapid development in the literature toward the understanding of cooling schemes made through AM means there is significantly more pressure loss and heat transfer data available in the literature

compared to a few years ago. The predictability of pressure loss or heat transfer of these cooling designs can be improved through additional data and a better understanding of the dominant factors that impact overall cooling performance. This study adds to the available data in the literature through the fabrication of cooling samples at a range of AM build conditions (build direction, channel size, and location) and improves on the capabilities for correlations to predict the pressure loss and heat transfer of the present samples and those in the literature. By using roughness statistics to correlate pressure loss and heat transfer, the developed correlations can be used regardless of changes to future laser process parameters, materials, and general AM build considerations.

Literature Review

It is important to characterize the surface roughness since there is a multitude of AM process and build conditions that impact the as-built surface roughness, such as changes to build direction [1,3], laser process parameters [4], part geometry [5], and location on the build plate [6,7]. Each of the aforementioned build conditions can change the shape of the roughness features and impact the relationships in cooling performance between samples. More specifically, the range in roughness features can be large dross

elements ranging from 25 μm to 75 μm [8] to smaller partially sintered particles less than 10 μm [9].

In microchannel cooling schemes, the length scales of the roughness features are the primary drivers of cooling performance [2]. The work by Kandlikar et al. [10] advocates that the roughness features can also be considered as a flow constriction, thus limiting the cross-sectional area, which needs to be accounted for in velocity calculations through the use of a constricted flow diameter term. Through the work by Stimpson et al. [2], certain roughness features can act as protruding fins into the flow field. Some roughness features (e.g., partially sintered particles) can have poor fin efficiency as a result of a high conduction resistance between the roughness feature and the AM surface. The results from Stimpson et al. [2] and Kandlikar et al. [10] highlight the importance of evaluating the roughness in order to understand and predict the cooling performance.

The foundational work of Nikuradse [11] used the term equivalent sand grain roughness, k_s, as a length scale for roughness in pressure loss (i.e., friction factor) correlations. However, the sand grain roughness is a scaling factor that is not directly measured; instead, it is determined through experiments. Since the study of Nikuradse [11], multiple roughness statistics such as arithmetic mean roughness (R_a), root mean square roughness (R_q), mean roughness depth (R_z), skewness (R_{sk}), and kurtosis (R_{ku}) are now used to describe the form of the surface morphology through destructive and nondestructive evaluation methods that were not previously available. Literature [2,10,12–18] uses these statistics along with other forms to correlate the roughness to the sand grain roughness in order to predict pressure loss and heat transfer in both nonadditive and additive cooling schemes. The early predictive work by Sigal and Danberg [19] used other statistical parameters to describe roughness in the form of a density parameter, Λ_s, for uniformly shaped roughness features using surface area ratios of the roughness elements to correlate sand grain roughness. Van Rij et al. [16] expanded upon this work by using the density parameter with three-dimensional irregular and nonuniform roughness features to predict sand grain roughness. Taking a different direction, Flack and Schultz showed that a combination of R_q and R_{sk} can be used to predict the sand grain roughness in the form of the Colebrook friction factor correlation with different types of roughness features (ranging from closely packed pyramids to spheres). However, these correlations struggle to predict cooling for AM datasets because the roughness magnitude-to-channel size ratio of these nonadditive studies is lower compared to the roughness nonuniformity and magnitude observed in AM parts.

Stimpson et al. [2] tackled this issue by comparing several roughness correlations in the literature to predict pressure loss and heat transfer using AM coupons from Stimpson et al. [20]. Of the many parameters evaluated, the study found that the arithmetic mean roughness-to-diameter ratio, R_a/D_h, best correlated to the relative sandgrain roughness, k_s/D_h. Furthermore, the study [2] also produced a modified Gnielinski Nusselt correlation exclusively for AM cooling schemes. It is important to note that the correlation was created using square and rectangular channels at a single build direction. Since then, additional data with multiple different channel shapes, build directions, and other AM build parameters have been reported in the literature. Several papers [2,12,13,21] have modified the coefficients of a similar form of the Stimpson et al. [2] equation by fitting additional datasets to better predict the relative sandgrain roughness in Colebrook's friction factor equation. In some cases in the literature [20,22–24], several AM coupons can contain a similar R_a/D_h ratio but exhibit different friction factors as well as Nusselt Numbers. As a result, using relative roughness correlations that are only a function of R_a/D_h struggle to predict the pressure loss or heat transfer for every sample. Goodhand et al. [15] highlight this predicament and state that R_a is a single roughness statistic that only describes the amplitude of the roughness elements.

A combination of roughness statistics is needed to better describe the relationship between the multiscale surface features to the pressure loss and heat transfer of AM cooling schemes. Using the additional datasets in the literature not present several years ago, the objective of the current study is to more accurately predict the pressure loss and heat transfer of AM cooling schemes. In addition to the data from the literature, several samples were fabricated at different build directions, locations, and diameters to be representative of major build parameters that impact cooling performance. The beginning of the paper describes the characterization in roughness and cooling performance and highlights the challenge with R_a/D_h to predict friction factor and Nusselt number. Toward the end of the paper, both the new data presented and data from the literature are used to predict pressure loss and heat transfer for a variety of samples using a combination of roughness statistics.

Description of Test Coupons

Twenty-seven cooling coupons, as seen in Table 1, were additively manufactured containing a range of different AM build parameters (build direction, build location, and channel size) that represent a variety of typical build and layout considerations of AM cooling schemes. A round channel was chosen for the coupons in Table 1 since stress concentrations during the AM process can occur at sharp corners such as square channel shapes leading to warpage. It is well known that the distance a laser is from the part surface can impact both geometry and cooling performance since the angle between the laser and normal to the surface (laser incidence angle) can impact the melt pool during the AM process [6]. As seen by the build plate of the coupons in Fig. 1, samples were printed at three specific radial build locations from the laser source (R1 = 25 mm, R2 = 58 mm, R3 = 90 mm) for each quadrant of a four-laser direct metal laser sintering EOSM400-4 machine. Even though the laser incidence angle changed as a result of the different radial build locations, literature has shown that the difference in surface roughness of a sample printed at different quadrants of a four-laser machine is minimal [25].

For each radial build location, samples were fabricated at three different build directions (0 deg, 45 deg, and 90 deg), where build direction is defined as the angle between the streamwise axis of the channel to that of the build plate, as seen in Fig. 1. Additionally, for each build direction the hydraulic diameter of the channel ranged from 0.8 mm to 1.4 mm. Circular channels were chosen for samples built at 90 deg due to no downward-facing surfaces, while samples built at a 45 deg and 0 deg build direction contained a teardrop correction to mitigate deformation at the downward-facing surface [3,26]. As seen in Fig. 2, the teardrop shape contained an apex angle of 120 deg. The samples were fabricated using STAL15DE [27] in a 40 μm layer thickness. After fabrication, the samples were solution annealed to reduce residual stress, and support removal was performed using a wire electrical discharge machine.

The geometric lengths of the coupons, specifically the channel pitch spacing (S), were varied for each hydraulic diameter so that the fin efficiency of the wall between channels during heat transfer measurements is greater than 95% to achieve a constant surface temperature boundary condition. Furthermore, the length-to-hydraulic diameter ratios of the coupons were between $35 < L/D_h < 61$ to meet fully developed flow conditions. The overall channel geometry for each coupon is reported in Table 1. The naming convention of the coupons in Table 1 describes the as-built diameter, channel shape, build direction, and radial build location. For example, as seen in Table 1, the 1.1-mm diameter sample containing a circular channel shape built at a 90-deg build direction at the third radius is named 1.1C90-R3.

Geometry Characterization

Accurately evaluating the as-built geometry of additively manufactured cooling schemes is important when quantifying pressure loss and heat transfer relations. Additionally, a comparison

Table 1 Geometries for coupons built at a variety of build directions, diameters, and locations as seen in Fig. 1

Coupon	Radial location (mm)	$D_{h,meas}$ (μm)	Build direction (deg)	Channel shape	$\dfrac{D_{h,meas}}{D_{h,des}}$	$\dfrac{P_{meas}}{P_{des}}$	$\dfrac{A_{c,meas}}{A_{c,des}}$	$\dfrac{S}{D_{h,des}}$	$\dfrac{L}{D_{h,des}}$
1.4C90-R1	R1 = 25	1405	90	Circle	1.004	1.064	1.068	1.57	35.2
1.4T45-R1	R1 = 25	1393	45	Teardrop	0.995	1.029	1.024	1.57	35.0
1.4T0-R1	R1 = 25	1350	0	Teardrop	0.964	1.019	0.982	1.57	35.0
1.1C90-R1	R1 = 25	1127	90	Circle	1.024	1.073	1.099	1.65	44.6
1.1T45-R1	R1 = 25	1118	45	Teardrop	1.016	1.039	1.056	1.65	44.6
1.1T0-R1	R1 = 25	1069	0	Teardrop	0.971	1.015	0.986	1.65	44.6
0.8C90-R1	R1 = 25	822.1	90	Circle	1.028	1.093	1.123	1.86	61.3
0.8T45-R1	R1 = 25	819.1	45	Teardrop	1.024	1.048	1.074	1.86	61.3
0.8T0-R1	R1 = 25	785.2	0	Teardrop	0.982	1.024	1.005	1.86	61.3
1.4C90-R1	R2 = 58	1438	90	Circle	1.027	1.054	1.083	1.57	35.0
1.4T45-R1	R2 = 58	1432	45	Teardrop	1.023	1.037	1.061	1.57	35.0
1.4T0-R2	R2 = 58	1341	0	Teardrop	0.958	0.988	0.946	1.57	35.0
1.1C90-R2	R2 = 58	1128	90	Circle	1.025	1.065	1.092	1.65	44.5
1.1T45-R2	R2 = 58	1112	45	Teardrop	1.011	1.023	1.034	1.65	44.6
1.1T0-R2	R2 = 58	1057	0	Teardrop	0.961	1.016	0.977	1.65	44.6
0.8C90-R2	R2 = 58	833.1	90	Circle	1.041	1.077	1.121	1.86	61.3
0.8T45-R2	R2 = 58	819.0	45	Teardrop	1.024	1.034	1.059	1.86	61.3
0.8T0-R2	R2 = 58	765.4	0	Teardrop	0.957	1.023	0.979	1.86	61.3
1.4C90-R3	R3 = 90	1415	90	Circle	1.011	1.066	1.078	1.57	35.0
1.4T45-R3	R3 = 90	1396	45	Teardrop	0.997	1.033	1.030	1.57	35.1
1.4T0-R3	R3 = 90	1347	0	Teardrop	0.962	1.017	0.978	1.57	35.0
1.1C90-R3	R3 = 90	1123	90	Circle	1.021	1.075	1.097	1.65	44.6
1.1T45-R3	R3 = 90	1116	45	Teardrop	1.014	1.043	1.058	1.65	44.6
1.1T0-R3	R3 = 90	1057	0	Teardrop	0.961	1.016	0.976	1.65	44.6
0.8C90-R3	R3 = 90	834.8	90	Circle	1.044	1.094	1.142	1.86	61.3
0.8T45-R3	R3 = 90	824.7	45	Teardrop	1.031	1.051	1.084	1.86	61.3
0.8T0-R3	R3 = 90	778.1	0	Teardrop	0.973	1.020	0.992	1.86	61.3

between the design intent and as-built geometry using evaluation methods provides insights into the printability of a design. A nondestructive evaluation method, specifically computed tomography (CT) scanning, was used to quantify the internal channel geometries of the coupons in Table 1 and check for channel blockages and overall deformation. The entire internal surface of the coupons was CT scanned at a 35 μm voxel resolution. The software was then used to determine the internal surface by filtering the grayscale values from the CT scan measurements [28]. Through interpolation, the CT scan software is capable of resolving one-tenth of the original voxel resolution [29].

Geometric dimensions such as hydraulic diameter, cross-sectional area, and perimeter of the channels were averaged and calculated using multiple cross-sectional slices taken from CT scan data along the streamwise axis of the channels. The specific details of this method have been extensively reported in the literature [22,23]. All geometric measurements and cooling performance parameters were calculated using CT scan data. The as-built geometric dimensions of the coupons from Fig. 1 are nondimensionalized by the design intent and are reported in Table 1. A graphical representation of the deviation of hydraulic diameter from the design intent is shown in Fig. 3 for the third radius samples.

The majority of the 45-deg teardrop and 90-deg circular samples printed larger than their design intent; however, the overall deviation from design intent for all the samples, regardless of build direction, was within 4%. For the 0 deg teardrop channels, their as-built
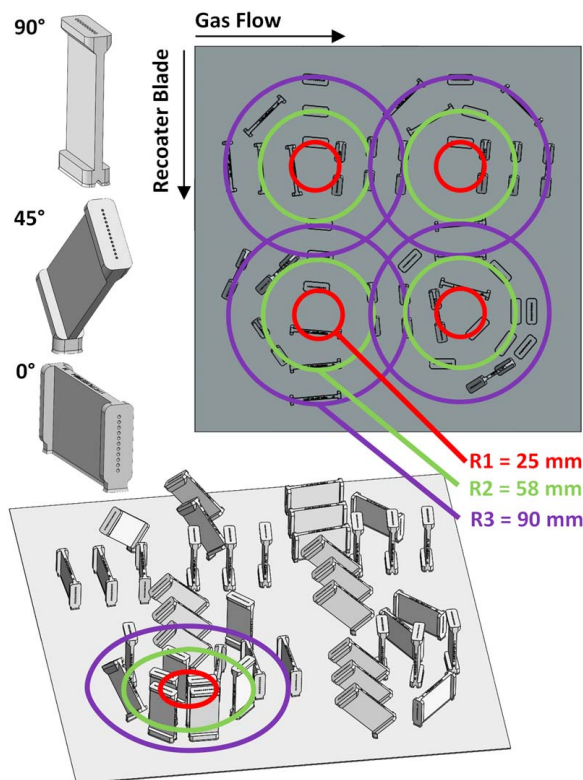

Fig. 1 Coupons spanning a range of build directions and diameters fabricated at three distinct radial locations from the four-laser EOS M400-4 machine
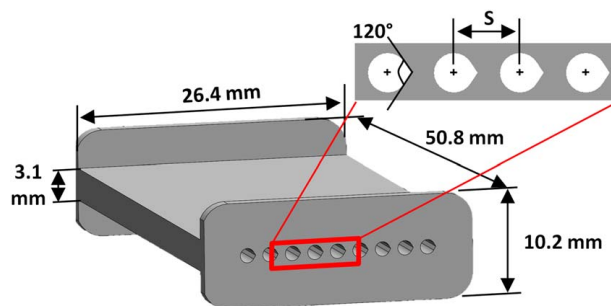

Fig. 2 Schematic of overall coupon dimensions used for experimental testing
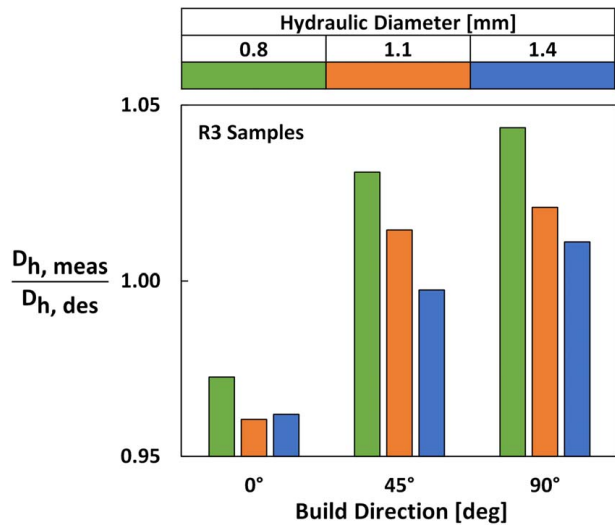
Fig. 3 Deviation from design intent hydraulic diameter of circular and teardrop channels at a range of build directions

hydraulic diameter is lower than their design intent. When examining the effect of diameter on deviation from design intent, decreasing diameter results in a higher deviation from the design intent for the 90-deg and 45-deg samples. As a result, the smallest channels (0.8 mm) exhibit the highest deviation from design intent at the 45-deg and 90-deg build direction relative to the other channel diameters. As seen in Table 1, changes to the radial build location of samples did not impact the deviation from design intent for specific diameter or build direction. This result is similar to vertically oriented square channels from Wildgoose and Thole [30] fabricated using a single laser machine.

As observed in Table 1, the as-built perimeter is, on average, 4% higher than the design intent for every sample besides the 1.4T0-R2, while for most samples, the as-built cross-sectional area follows the same build direction trends as the deviation from the hydraulic diameter in Fig. 3.

Roughness Characterization

Surface morphology has a direct influence on the amount of turbulent mixing, resulting in changes to pressure loss and convective heat transfer. Evaluating surface roughness and its impact on cooling performance aids in the understanding and predictive capabilities of pressure loss and heat transfer in highly rough additive cooling schemes. Surface roughness statistics, such as the arithmetic mean roughness, R_a, were quantified for the internal surfaces nondestructively using the same CT scan data to calculate channel geometries. The arithmetic mean roughness describes the average deviation of the surface features from a reference value (this is typically the mean roughness height).

Since the shape of the channels contained curved surfaces (circular and teardrop), an ellipsoid was fitted using a linear least square regression method to each axial cross-sectional slice along the channel length. The average difference from the channel surface to the fitted ellipse was recorded as the arithmetic mean roughness, R_a. The arithmetic mean roughness values in Fig. 4 were averaged from multiple channels in each of the coupons in Table 1. The method for calculating arithmetic mean roughness is similar to a method used by Klingaa et al. [31] for highly curved channel shapes.

As seen in Fig. 4(a), samples fabricated at the 90-deg build direction show the lowest arithmetic mean roughness level relative to the 45-deg and 0-deg orientations. There is no dependence of radial build location on arithmetic mean roughness for any of the build directions. As a result, only the third radius samples from Table 1

are shown in Fig. 4. This result is in contrast to the literature [6,7,25]. The cause for no difference in surface roughness as a function of radial location is a factor of the smaller difference in laser incidence angle between the samples fabricated on a four-laser machine relative to the samples in the literature fabricated on a single laser machine. The change in laser incidence angle is smaller for samples on the four-laser machines due to a smaller radial location compared to samples built using a single laser machine in previous literature. At most of the build directions, samples with the highest diameter (1.4 mm) also show the highest arithmetic mean roughness regardless of radial build location.

Nondimensionalizing the arithmetic mean roughness by hydraulic diameter reveals the scale of the roughness features relative to channel size. The results in Fig. 4(b) show that as the diameter decreases, so does the roughness-to-diameter ratio. The 0.8-mm samples are, on average, 15% higher in their relative roughness compared to the 1.1-mm and 33% higher compared to the 1.4-mm samples averaged across all build directions and build locations. There is an average 24% increase in roughness–to-diameter ratio between the 90-deg and 0-deg build direction for the 0.8-mm samples. The roughness-to-diameter ratio is not a function of build location. Additionally, the roughness-to-diameter ratio increases from the 90-deg to 0-deg build direction for a given diameter, which is similar to results reported by Snyder et al. [3] and Wildgoose et al. [23]. The cause for this is related to the increasing deformation at the downward-facing surfaces.
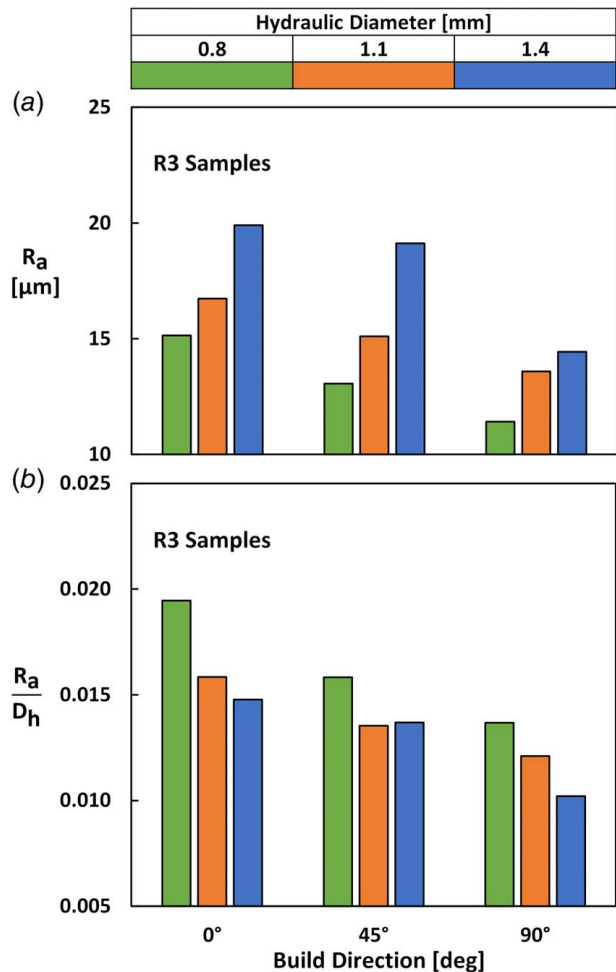

Fig. 4 Arithmetic mean roughness (a) and relative roughness (R_a/D_h) (b) of samples for a range of diameters at different build directions and radial build locations

Channel Performance Measurements

The pressure loss and bulk convective heat transfer of the samples were experimentally measured using a rig, shown in Fig. 5, which has been extensively reported in the literature and benchmarked [2,23]. The friction factor was measured over a range of Reynolds numbers covering the transitional and fully turbulent regime by measuring the static pressure drop between the inlet and outlet of the coupon. Mass flowrate and the geometry of the channels measured from CT scans were accounted for in the friction factor measurement. More specifically, the mass flowrate was measured upstream of the samples using a laminar flow element. The backflow pressure was regulated downstream of the sample to achieve fully turbulent Reynolds numbers while also being in the incompressible regime (Mach number < 0.2). Since the static pressure measurements are upstream of the sample, an inlet loss coefficient was calculated using an area ratio (between the plenum inlet and the sample cross-sectional area), while the outlet loss coefficient was one, as referenced in Munson et al. [32].

Using the same test rig in Fig. 5, bulk convection coefficients were measured by imposing a constant surface temperature boundary condition using a heater placed on either side of the coupon with a copper block (imbedded with thermocouples) between the coupon and heater. A one-dimensional conduction circuit using the thermocouples inside the copper block was evaluated to measure the surface temperature of the channels inside the coupon. Stimpson et al. [2] report a more detailed description of the heat transfer method.

Thermocouples inside the rigid foam and plenums measured conduction losses, and these losses were accounted for in the heat transfer measurements. The total conduction losses were less than 1% of the total power supplied by the heaters across the range of Reynolds numbers evaluated. A separate analysis was performed to account for the losses. The difference between the amount of heat supplied by the heaters, $Q_{heaters}$, to that of the heat transported by the air, Q_{air}, after accounting for the conduction losses, was 3% at the lowest Reynolds numbers and within 2% at the highest Reynolds number for all the samples evaluated.

Experimental Uncertainty

The propagation of uncertainty method following the procedure outlined in Figliola and Beasley [33] was used to determine the experimental uncertainty in friction factor and Nusselt number. The largest contributors to the uncertainty in the friction factor were the hydraulic diameter and pressure drop. The uncertainty in friction factor was 5% at the lowest Reynolds numbers, while it was 4% at the highest Reynolds numbers. The uncertainty in the Reynolds number for all the samples was less than 5%. For the heat transfer tests, specifically measuring the Nusselt number, the thermocouple exit temperatures, and hydraulic diameter contributed most to the uncertainty in the Nusselt number. The experimental uncertainty for the Nusselt number was 7% across the range of Reynolds numbers evaluated.
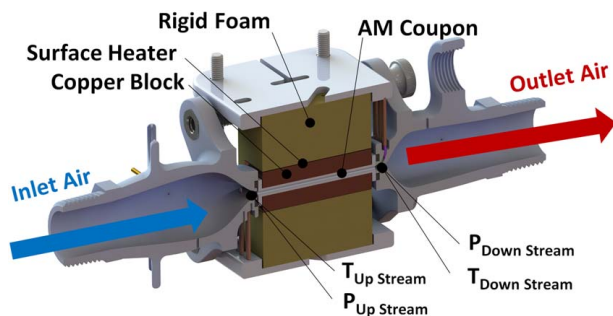

Fig. 5 Schematic of experimental rig used to measure pressure loss and heat transfer

Pressure Loss Measurements

To compare the pressure loss between samples, the nondimensional friction factor was measured over a range of transitional and fully turbulent Reynolds numbers, as shown in Fig. 6, for all the samples in Table 1. Also included in Fig. 6 is the benchmark data for the experimental rig, where the friction factor of a smooth circular channel coupon agrees with the well-known Colebrook friction factor equation, Eq. (1), at a sandgrain roughness of zero.

$$\frac{1}{\sqrt{f}} = -2\log_{10}\left(\frac{K_s}{3.7 D_h} + \frac{2.51}{Re\sqrt{f}}\right) \tag{1}$$

For most of the samples in Fig. 6, the friction factor becomes fully turbulent at around a Reynolds number of 7500 (critical Reynolds number). As the magnitude of the friction factor increases, the critical Reynolds number decreases. Similar to the roughness results in Fig. 4(a), the friction factor is highest for the smallest diameter channel, which is most likely due to the increase in the roughness-to-diameter ratio, as seen in Fig. 4(b). The highest level of friction factor was for the 0.8C90-R2 sample, which was 87% different compared to the sample (1.4T0-R2) with the lowest friction factor at a Reynolds number of 10,000. For most of the diameters evaluated, changes to the radial build location did not impact the friction factor. The average difference in friction factor between radial build locations was 7% for the 0.8-mm samples, 10% for the 1.1-mm samples, and 10% for the 1.4-mm samples across all the build directions.

To clearly view trends in friction factor between datasets in Fig. 6, friction factor augmentation as a function of build direction for the samples in Table 1 at a fully turbulent Reynolds number of 20,000 is shown in Fig. 7, where friction factor is augmented by the friction
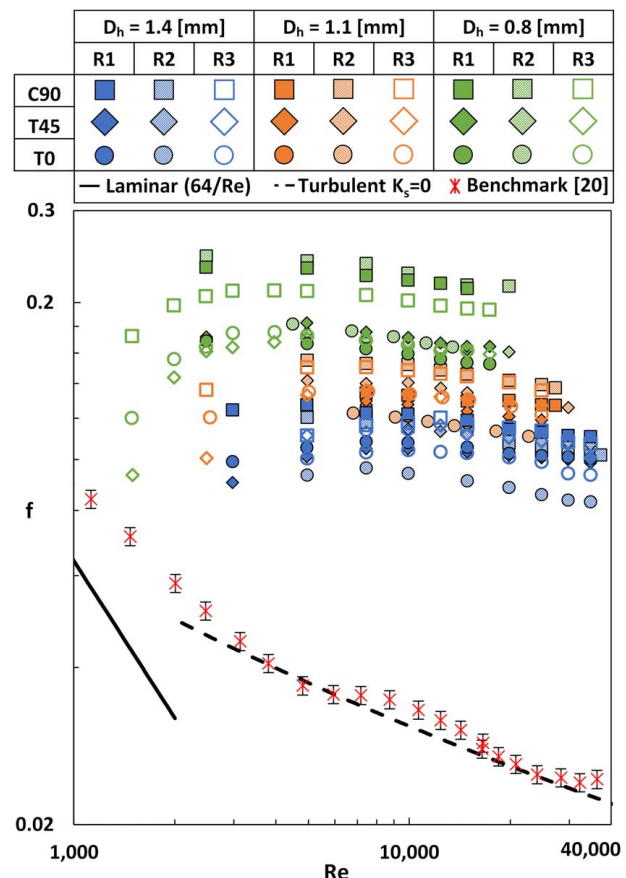

Fig. 6 Friction factor of coupons from Table 1 built over a wide range of build directions, build locations, and diameters
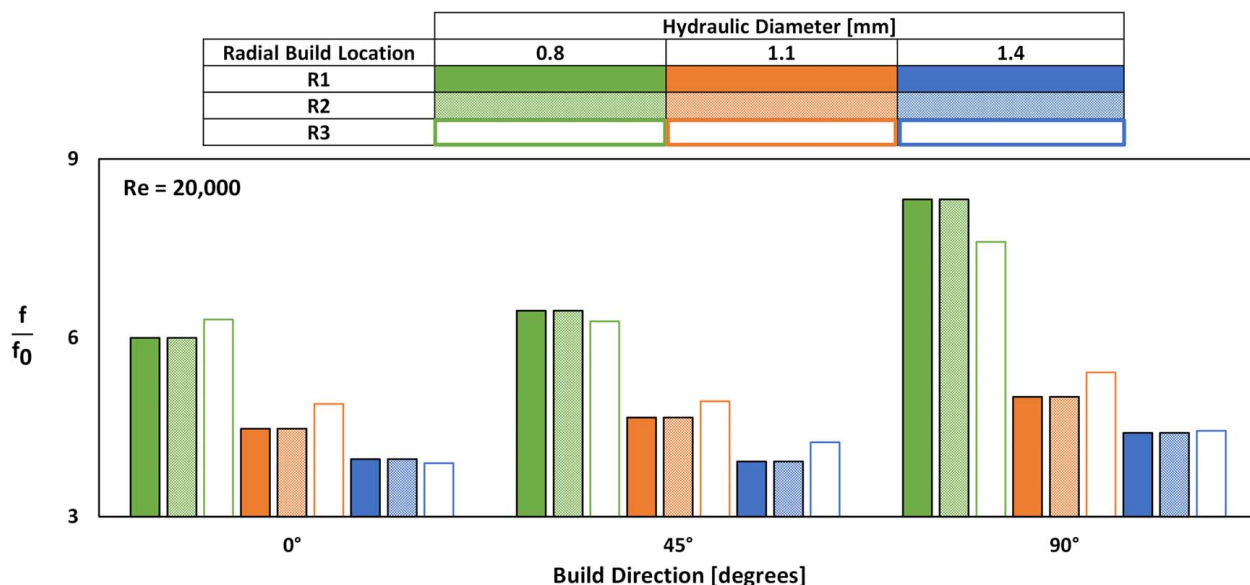
Fig. 7 Friction factor augmented by the friction factor of a hydraulically smooth channel at a Reynolds number of 20,000 for the samples in Table 1

factor of a hydraulically smooth channel (sandgrain roughness equal to zero) calculated using the Colebrook equation at a shared Reynolds number. For any given diameter, the vertically oriented channels (C90) exhibit the highest friction factor, while in some cases, the 0-deg and 45-deg channels share a similar friction factor augmentation. Additionally, the lowest diameter (0.8 mm) samples showed a greater difference in friction factor augmentation between build directions compared to the other diameters. In more detail, the friction factor augmentation of the 90-deg 0.8-mm channels is 23% higher relative to their 45-deg and 0-deg equivalents, while the 1.1-mm diameter 90-deg samples (averaged across all build locations) contained an 11% higher friction factor augmentation compared to their 0-deg and 45-deg equivalents. Lastly, the 1.4-mm diameter 90-deg samples were 9% higher in their friction factor augmentation compared to the 0-deg and 45-deg samples.

The friction factor augmentation follows different trends compared to the roughness-to-diameter ratio in Fig. 4(*b*). While the 90-deg samples contained the lowest roughness-to-diameter ratio, their friction factor augmentation was among the highest compared to all other build directions. Consequently, the roughness-to-diameter ratio struggles to capture the pressure loss trends between samples in Fig. 7. In a more detailed example, the friction factor augmentation increases 29% for the R3 0.8-mm samples when going from 45-deg to the 90-deg build direction, while the roughness-to-diameter ratio for the same R3 samples decreases 12% when going from 45 deg to 90 deg.

Heat Transfer Measurements

Similar to the friction factor tests, the Nusselt number was measured over a range of fully turbulent Reynolds numbers, as seen in Fig. 8. Also included in Fig. 8 are benchmark data from the same hydraulically smooth cylindrical channel coupon as the benchmark data in Fig. 6. The benchmark data in Fig. 8 agree with the well-known Gnielinski Nusselt correlation calculated using a hydraulically smooth friction factor.

The difference in Nusselt number between samples is less than the difference in friction factor. In more detail, there is a 23% difference in Nusselt number between the samples at a Reynolds number of 20,000, while for friction factor, the difference is 84% at the same Reynolds number. Both the 0.8T0-R2 and 0.8C90-R2 samples showed the highest Nusselt number, while the 1.4C90-R3 and 0.8T45-R1 exhibited the lowest Nusselt number

for the range Reynolds numbers. When comparing the heat transfer performance between build locations in Fig. 8, samples at the second radius contain the highest Nusselt augmentation, followed by the third radius and then the first radius across most of the build directions. However, the overall trends with build direction and diameter between build locations are the same.

To more easily view trends between the Nusselt numbers of the samples in Fig. 8, Nusselt augmentation of the three radial locations at a shared fully turbulent Reynolds number of 20,000 is shown in Fig. 9. More specifically, the Nusselt number is augmented by the Nusselt number of a hydraulically smooth channel calculated using the Gnielinski correlation with a sandgrain roughness of zero. In contrast to the results from Figs. 4 and 7, Nusselt augmentation does not increase with decreasing channel diameter at any given radial location. Furthermore, the trends in Nusselt number augmentation between samples do not follow friction factor trends. For some samples, such as the 0.8T45-R3 coupon, the Nusselt augmentation is the lowest, even though the friction factor augmentation in Fig. 7 was the highest for the 45-deg samples. Similar results were observed in coupons fabricated over a wide range of build directions by Wildgoose et al. [23], where certain roughness elements contributed greatly to pressure loss but contained poor fin efficiencies, resulting in a lower Nusselt number relative to friction factor. Samples oriented in the 90-deg build direction exhibit a similar or lower Nusselt augmentation as samples at the 0-deg or 45-deg build direction.

The arithmetic mean roughness-to-diameter ratio does not follow the Nusselt augmentation trends in Fig. 9. When examining the R3 samples, the Nusselt augmentation for the R3 samples at the 45-deg build direction in Fig. 9 increases when going from 0.8 mm to 1.4 mm, while for the same R3 samples in Fig. 4(*b*), the roughness-to-diameter ratio decreases going from 0.8 mm to 1.4 mm. Another example is that both the 1.1T0-R3 and 1.4T0-R3 samples share the same Nusselt augmentation while exhibiting a 27% difference in arithmetic mean roughness-to-diameter ratio. The differences in trends between Figs. 9 and 4(*b*) highlight the challenge of using only R_a/D_h to predict the Nusselt number or friction factor.

Pressure Loss Correlation

There can be a wide range of friction factors and Nusselt number values for the same arithmetic mean roughness, as has been shown

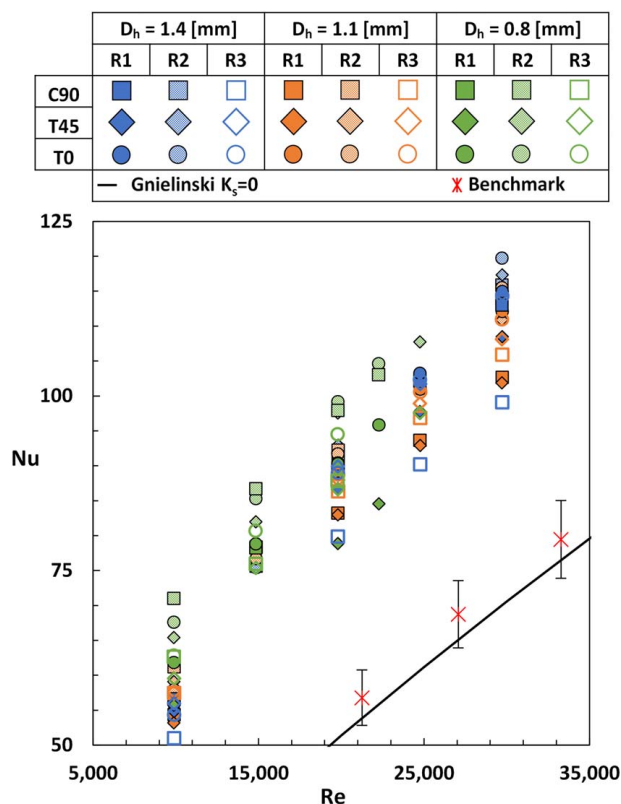|	$D_h = 1.4$ [mm]			$D_h = 1.1$ [mm]			$D_h = 0.8$ [mm]		
	R1	R2	R3	R1	R2	R3	R1	R2	R3
C90	◼	◼	◻	◼	◼	◻	◼	◼	◻
T45	◆	◆	◇	◆	◆	◇	◆	◆	◇
T0	●	●	○	●	●	○	●	●	○
— Gnielinski $K_s=0$							✗ Benchmark		

Fig. 8 Nusselt number of samples (with a variety of build directions, locations, and diameters) from Table 1 covering a range of turbulent Reynolds numbers

Noncircular channel shapes, such as square, rectangular, pentagonal, and trapezoidal, can exhibit a range of different roughnesses for each side of the channel. Thus, it is difficult for an area-averaged roughness statistic to fully capture the surface morphology of the channel. As highlighted by Wildgoose et al. [24], there can also be scaling issues in noncircular channel shapes as a result of using hydraulic diameter as the characteristic length in friction factor, Nusselt number, and Reynolds number.

The samples in Table 2 include both circular and teardrop channels built over a range of different build directions, materials, laser process parameters, channel diameters, machines, and different build locations. The present study reanalyzed samples with various roughness statistics from Snyder et al. [22], Wildgoose et al. [24], and Wildgoose et al. [23]. While there were additional samples in the literature [34,35] that met the criteria for the teardrop and circular channels, only a single roughness statistic, such as arithmetic mean roughness, was reported. It is important to recognize that as the AM cooling field grows, so does the need for additional surface roughness statistics to be reported with arithmetic mean roughness.

By focusing on correlating roughness to pressure and heat transfer, the correlations can be used regardless of changes to the machine or process parameters. Several approaches were taken in an effort to correlate the measured surface roughness of the samples in Table 2 to predict pressure loss. The first approach followed a similar method to Van Rij et al. [16] and Goodhand et al. [15], whereby CT scan data of the samples in Table 2 were used to calculate a statistical length parameter using the autocorrelation function (ACF). An ACF used on roughness measurements determines the similarity of a roughness profile. By selectively moving the roughness profile in discretized lengths, an ACF is then performed to determine the similarity between roughness elements at a given discretized length (also known as a lag). If values returned from the ACF are near one, then the surface profile is well correlated, while values less than one and even less than zero indicate the surface profile is not very well correlated. Goodhand et al. [15] observed that the minimum discretized length for which the ACF value is at 0.2 results in the roughness profile no longer being correlated, and the discretized length is statistically significant. Following a similar procedure as Goodhand et al. [15], the discretized length for which an ACF value is at 0.2 in a channel is known as the correlation length, λ. Several pieces in the literature [2,15] have attempted to correlate sandgrain roughness to the correlation length of both additive and nonadditive datasets. A

in previous sections. Consequently, AM correlations in the literature that rely solely on the arithmetic mean roughness-to-diameter ratio struggle to predict friction factor or Nusselt number. To solve this issue, the coupons presented in this paper, along with those reported in the literature, were used to develop a more accurate correlation between heat transfer and pressure loss of internal channels. The test matrix of samples, as seen in Table 2, in the literature was limited to circular or teardrop channel shapes.

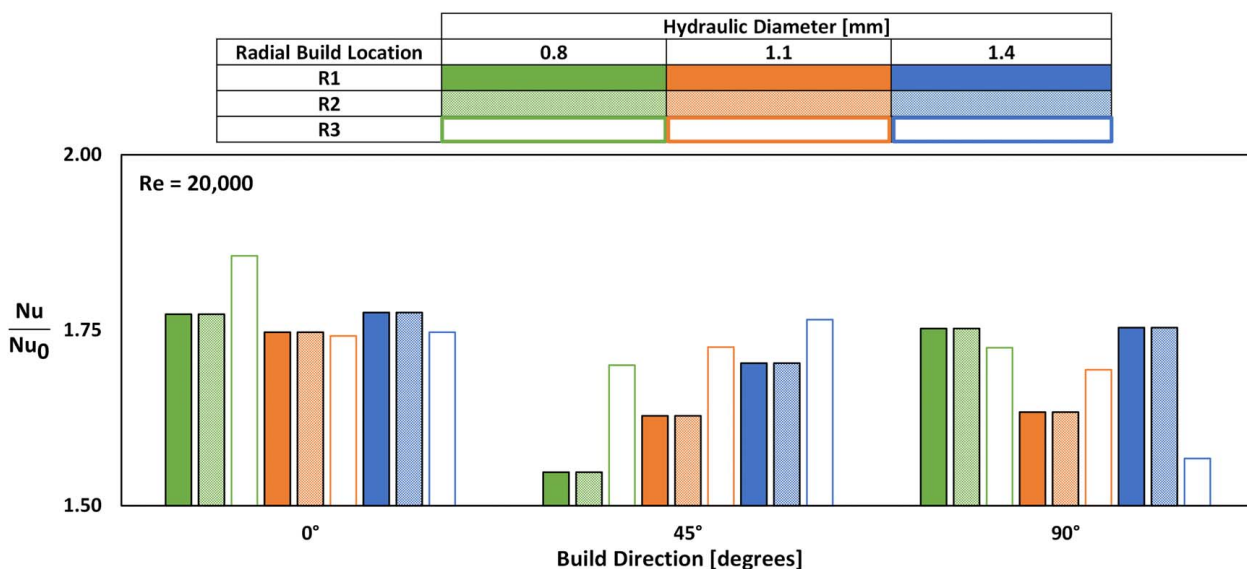| Radial Build Location	Hydraulic Diameter [mm]		
	0.8	1.1	1.4
R1	🟩	🟧	🟦
R2	🟩	🟧	🟦
R3	◻	◻	◻

Fig. 9 Nusselt augmentation of samples fabricated at a variety of build directions and diameters at R1, R2, and R3 at a shared Reynolds number of 20,000

Table 2 Samples used for comparing and generating friction factor and Nusselt number correlations

Channel shape	D_h (mm)	Build direction	R_a/λ	Λ_s	R_q/D_h	R_{sk}	No. of samples	Ref.
Circular	0.75–1.25	0–90	0.0026–0.1540	32–536	0.010–0.072	−0.25–0.46	13	[3]
Circular teardrop	0.51	45	0.0042–0.0551	25–206	0.013–0.048	−0.33–1.18	4	[23]
Circular	1.52	90	0.0844	313	0.009	−0.39	1	[24]
Circular teardrop	0.80–1.40	0–90	0.0104–0.1422	8–241	0.013–0.025	−0.6–0.59	27	Current study

correlation length was evaluated for each of the samples in Table 2, using CT scan data. A point cloud of the surface was generated using the cross-sectional slices from the CT scan data. The point cloud was then organized into multiple axial profile slices going into the channel (similar to a profile obtained by a stylus roughness probe). The ACF was recorded for each lengthwise slice, and the correlation length was calculated.

Additionally, the Sigal and Danberg [19] density parameter, Λ_s, was also calculated for all the samples in Table 2 since the parameter has seen success in predicting sandgrain roughness in nonadditive studies [16,17]. As seen in Eq. (2), the density parameter contains two area ratios. The left area ratio describes the surface area without roughness to that of the summed frontal projected area of the individual roughness elements, while the right area ratio describes the same frontal projected area to the summed total wetted frontal area of the roughness elements.

$$\Lambda_s = \left(\frac{A}{A_f}\right)\left(\frac{A_f}{A_w}\right)^{-1.6} \quad (2)$$

Following a similar procedure to calculate the area ratio as Forooghi et al. [17], a standard tessellation language (STL) of individual channels from samples in Table 2 was extracted from CT scan data. Using an in-house code, the STLs were organized where the cross-sections of a channel were placed on the x- and y-axis while the axial length was on the z-axis. For each triangle in the STL file, a normal vector (facing the interior of the channel) at the centroid of each triangle was determined. The wetted frontal area, A_w, was calculated by summing the area of all triangles whose normal vector (flow-facing triangle) faced the positive z-axis direction. The frontal area, A_f, was calculated by taking the area (projected) perpendicular to the flow for each of the flow-facing triangles. Normally, the CAD design intent of the channel would be used as the surface area without roughness features; however, because the AM process fundamentally changes the shape of the channel, the design intent is not representative of the as-built geometry. Consequently, the surface area without roughness, A, was calculated by taking the average perimeter from cross-sectional slices and multiplying it by the overall channel length.

A range of λ and Λ_s are provided in Table 2 for the different samples and shown in Fig. 10 as a function of sandgrain roughness nondimensionalized by the arithmetic mean roughness calculated from CT scans. Unlike the results from Goodhand et al. [15], the nondimensionalized correlation length struggles to correlate with the nondimensional sandgrain roughness in Fig. 10(a). Most notably, there is a wide range in k_s/R_a between samples for any given R_a/λ. At an R_a/λ value of 0.1, there can be up to a 120% spread in k_s/R_a between samples. A similar observation in the struggle of λ predicting k_s is stated by Snyder et al. [2].

The density parameter also struggles to correlate with the nondimensionalized sand grain roughness, as seen in Fig. 10(b). Accompanied in Fig. 10(b) is a piecewise correlation developed by Van Rij et al. [16]. When Λ_s is greater than 28, the correlation [16] decreases in k_s/R_a; however, the k_s/R_a for the AM datasets remains the same regardless of any change to Λ_s. Furthermore, the value of the nondimensionalized sandgrain roughness is higher than the correlation [16].

The second approach to correlate roughness to pressure loss, in this case, a nondimensionalized pressure loss known as friction factor, was performed by investigating different forms of bulk

roughness statistics, which included R_a, R_q, and R_{sk}. Bulk roughness statistics require less information on the surface compared to both λ and Λ_s and, therefore, are easier to measure. All basic roughness statistics were calculated using CT scan data with the fitted ellipsoid method. The skewness, R_{sk}, of the roughness represents the distribution of roughness elements relative to the mean. A positive value of skewness implies that the surface roughness contains more peaks (surface features are above the mean), while a negative skewness indicates most surface features represent valleys (surface features are below the mean roughness).

Several friction factor correlations for AM cooling schemes from the literature [2,13,21,34] are shown in Table 3 and were compared using the datasets from Table 2. The mentioned correlations predicted relative sandgrain roughness, k_s/D_h, using a measured relative arithmetic mean roughness, R_a/D_h. The predicted friction factor in Fig. 11 for the correlations by Stimpson et al. [2], Thole et al. [13], Mazzei et al. [21], and Molitor [34] was calculated by calculating the friction factor from Colebrook's equation, Eq. (1), using the predicted relative sandgrain roughness. Out of the 45 samples in Table 2 evaluated for the correlations from the literature in Table 3, three samples were omitted from the analysis since the R_a/D_h ratio was either an extremely high value ($R_a/D_h > 0.035$) such
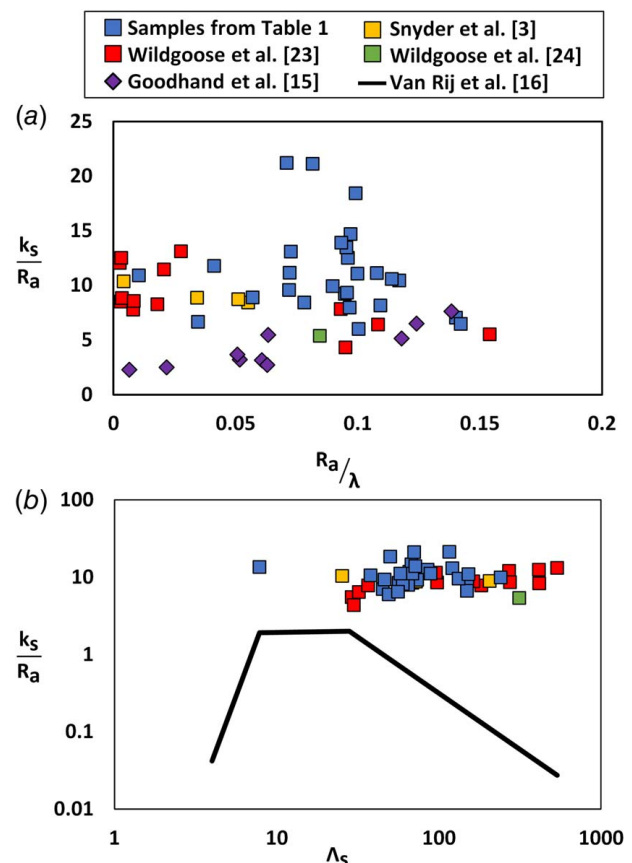

Fig. 10 Comparison of correlation length and density parameters to sandgrain roughness for the samples in Table 2

Table 3 Correlations for predicting friction factor of the samples in Table 2

Correlation	Avg |% Error|	Max |% Error|	Ref.
$\dfrac{k_s}{D_h} = 18\dfrac{R_a}{D_h} - 0.05$	31%	103%	[2]
$\dfrac{k_s}{D_h} = 11\dfrac{R_a}{D_h}$	15%	47%	[13]
$\dfrac{k_s}{D_h} = 25.247\dfrac{R_a}{D_h} - 0.0822$	68%	186%	[21]
$\dfrac{k_s}{D_h} = 5.094\dfrac{R_a}{D_h} + 0.0258$	21%	53%	[34]
$f = 2.6\dfrac{R_q}{D_h}(1 + R_{sk})^{0.3} + 0.074$	12%	25%	Eq. (3)

as the case for the 1.25-mm and 1-mm 0-deg circular coupons from Wildgoose et al. [23] or an extremely low R_a/D_h value ($R_a/D_h < 0.007$) such as the 1.5-mm circular channel diameter at a 90-deg build direction from Wildgoose et al. [24].

Figure 11 shows the difference between the predicted friction factor (f_{pred}) using the correlations in Table 3 to the friction factor measured through experiments (f_{exp}). More specifically, the Colebrook friction factor equation was used to calculate a predicted friction factor from the relative sandgrain roughness correlations in Table 3. As seen in Fig. 11, there is a wide range between the predicted and experimental friction factors for the correlations from the literature. As shown in Table 3, the average and maximum absolute percent error was calculated to compare how well the datasets in Table 2 were predicted. As seen in Fig. 11, both Stimpson et al. [2] and Mazzei et al. [21] tend to overpredict the friction factor, while the correlation from Molitor underpredicts the friction factor. One of the earliest correlations for AM datasets from Stimpson et al. [2] predicts the friction factor of the samples within an average of 31%; however, the maximum error can be up to 103%. Molitor [34] changed the coefficients of the same equation
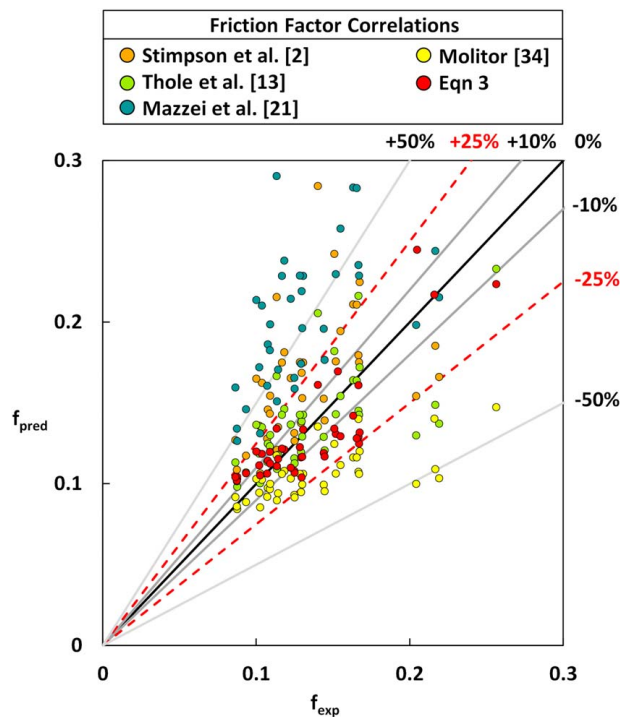
form as Stimpson et al. [2]. With the change in coefficients, the Molitor [34] correlation is able to predict a 21% average absolute percent error and 53% maximum absolute error. By removing the offset term from Stimpson et al. [2], the Thole et al. [13] correlation is able to further reduce the error in predicting friction factor with a 15% average absolute error and 47% maximum absolute error.

However, as was seen in the friction factor augmentation plot of Fig. 7 and the roughness-to-diameter ratio plot of Fig. 4(b), several samples can contain the same roughness-to-diameter ratio while containing different friction factors. The cause for the arithmetic mean roughness-to-diameter ratio struggling to be related to friction factor or Nusselt number is due to the surface morphology. The work of Stimpson et al. [2] proposes that certain roughness elements can contribute differently to pressure loss and heat transfer. Depending upon how well sintered the roughness element is to the surface can impact the fin efficiency of the roughness element. Partially sintered particles have poor fin efficiency due to a high conduction resistance between the roughness element and the AM surface. The ability to better describe the surface morphology is an ongoing area of research in the community. The use of multiple roughness parameters, instead of a single bulk roughness statistic (R_a) that does not fully describe the surface morphology, can help reveal trends in friction factor and Nusselt number. A more accurate prediction in friction factor using roughness terms is challenging to achieve by simply changing the coefficients of a similar form to Stimpson et al. [2].

A different approach was taken to correlate the samples in Table 1. Flack and Shultz [18] found that a combination of using the root mean square roughness, R_q, coupled with skewness, R_{sk}, resulted in the most effective method to predict sandgrain roughness for non-AM datasets. A similar approach to correlating roughness to pressure loss was taken for the samples in Table 2 as Flack and Schultz [18] to generate the correlation, as seen in Eq. (3).

$$f = 2.6\frac{R_q}{D_h}(1 + R_{sk})^{0.3} + 0.074 \qquad (3)$$

However, friction factor was correlated instead of sandgrain roughness and to nondimensionalize the equation, the root mean square roughness is normalized by the as-built hydraulic diameter. By calculating the friction factor directly, the process of going through a friction factor correlation, such as Colebrook, is bypassed. Four samples out of the forty-five in Table 2 were omitted from the best fit for Eq. (3). Specifically, the 0.8-mm 90-deg samples built across the different locations from the current study were omitted due to being outliers as a result of the highest friction factor relative to other samples. Furthermore, the 1.5-mm circular channel from Wildgoose et al. [24] was left out due to a significantly lower R_q/D_h value relative to the other datasets. As seen in Eq. (3) and Table 3, the friction factor correlation is able to predict the data from Table 2 within a 12% average absolute error and 25% maximum absolute error. As seen in Fig. 11, most samples predicted from Eq. (3) are less than 10% error. The use of multiple roughness statistics in Eq. (3) results in half the amount of maximum error as the most accurate R_a/D_h correlation (from Thole et al. [13]).

The friction factor correlation, Eq. (3), consists of samples fabricated at different AM machines, channel sizes, materials, build directions, and radial build locations. It is important to note that Eq. (3) is only valid for curved channel shapes such as circular and teardrop shapes. Furthermore, the correlation is only valid in the fully turbulent regime, where the friction factor does not change with the Reynolds number.

A comparison of friction factor for several datasets from Table 2 and a noncircular channel shape from Wildgoose et al. [24] is shown in Fig. 12. As seen in Fig. 12, Eq. (3) is more effective at predicting the friction factor relative to the other correlations in Table 2 between the different datasets. However, as mentioned, Eq. (3) struggles to predict noncircular channel shapes, such as the pentagon in Fig. 12. The cause is that the positive or negative
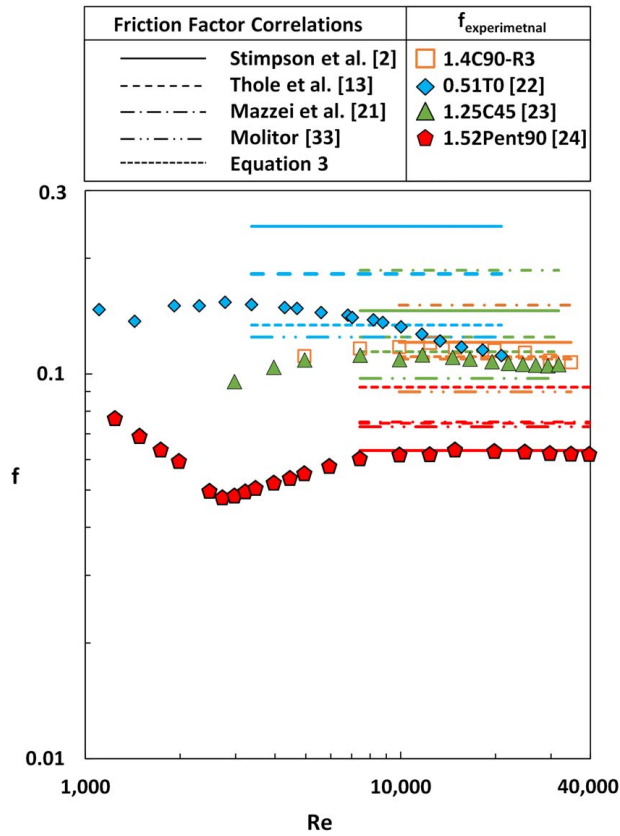

Fig. 11 Experimental friction factor compared to friction factor predicted using the correlations in Table 3 of the datasets in Table 2

Fig. 12 Comparison of friction factor correlations of select samples from Table 2

value of the skewness term is filtered out when performing an area average skewness for each surface of the pentagon channel.

Heat Transfer Correlation

In addition to correlating friction factors, several Nusselt number correlations for the datasets in Table 2 were also investigated. More specifically, a modified Gnielinski correlation from Stimpson et al. [2] was compared to another modified form of the Gnielinski correlation, Eq. (4), which was fitted using the data in Table 2. The same datasets used to make the friction factor correlation, Eq. (3), were used to generate the Nusselt number correlation, Eq. (4). Both Nusselt number correlations, in Table 4, are functions of Reynolds number, friction factor, and Prandtl number. The predictions of both correlations are presented in Fig. 13 with two approaches toward calculating the Nusselt number. The first approach assumed that the friction factor is known and both Nusselt correlations were calculated using the friction factor measured from experiments, while the second approach assumed that the friction factor is unknown and is predicted using a friction factor correlation, Eq. (3).
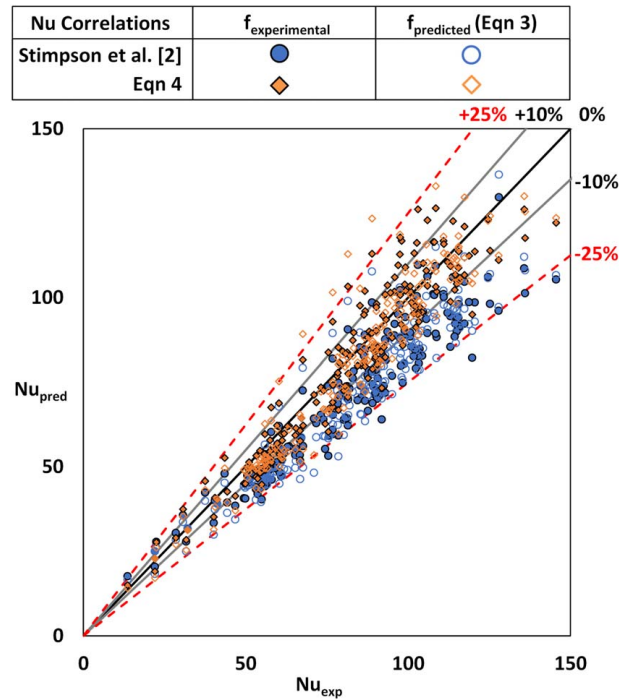

Fig. 13 Experimental Nusselt number of samples from Table 2 compared with the predicted Nusselt number using the experimental friction factor and friction factor predicted using Eq. (3).

The difference from the predicted Nusselt number (Nu_{pred}) using the correlations in Table 4 to the Nusselt measured through experiments (Nu_{exp}) is shown in Fig. 13. In more detail, the experimental Nusselt number at a variety of Reynolds numbers for each coupon is compared to a predicted Nusselt number using two different Nusselt number correlations. As seen in Fig. 13 and Table 4, Eq. (4) is more effective at predicting the Nusselt number using the experimental friction factor and predicted friction factor compared to the Stimpson et al. [2] correlation.

$$Nu = \frac{(Re^{0.477} - 31)Pr\sqrt{f/8}}{0.38(1 - Pr^{2/3})} \qquad (4)$$

When using Eq. (4), the average absolute error is reduced by half compared to the Stimpson et al. [2] correlation, as seen in Table 4. As seen in Fig. 13, the Stimpson et al. [2] correlation underpredicts the Nusselt number when using the experimental friction factor and predicted friction factor. As seen in Table 4, there is minimal difference between using the experimental or predicted friction factor for the average and maximum error of the Stimpson et al. [2] correlation. Despite Eq. (4) exhibiting a higher maximum error using the predicted friction factor compared to Stimpson et al. [2], there is a single outlier in the data that contributes to the higher maximum error. By removing the outlier (1-mm channel built at the 0 deg build direction) from Wildgoose et al. [23] in the

Table 4 Correlations for predicting heat transfer of the samples in Table 2

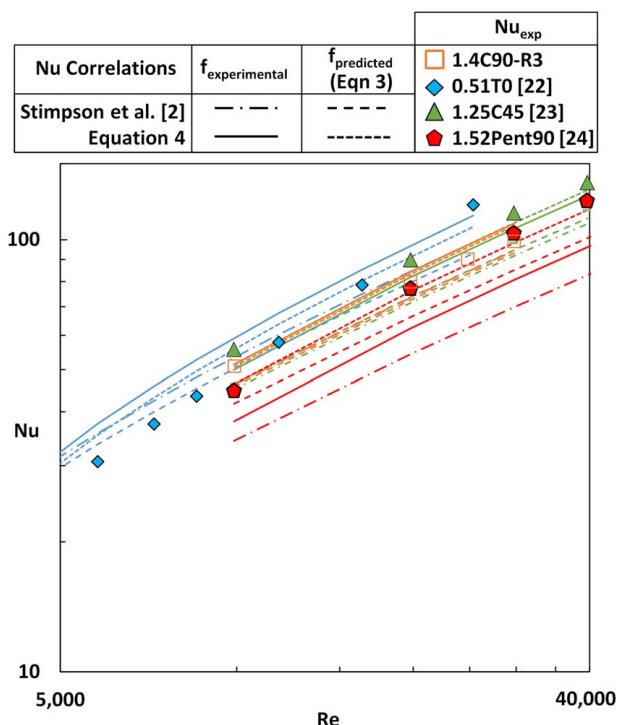| Correlation	f_{exp}		f_{pred} (Eq. (3))		
	Avg |% Error|	Max |% Error|	Avg |% Error|	Max |% Error|	Ref.
$Nu = \dfrac{(Re^{0.5} - 29)Pr\sqrt{f/8}}{0.6(1 - Pr^{2/3})}$	14%	31%	16%	32%	[2]
$Nu = \dfrac{(Re^{0.477} - 31)Pr\sqrt{f/8}}{0.38(1 - Pr^{2/3})}$	8%	27%	8%	39%	Eq. (4)

Nu Correlations	$f_{experimental}$	$f_{predicted}$ (Eqn 3)	Nu_{exp}	
			□ 1.4C90-R3	
Stimpson et al. [2]	— · —	– – –	◆ 0.51T0 [22]	
Equation 4	——	-------	▲ 1.25C45 [23]	
			⬠ 1.52Pent90 [24]	

Fig. 14 Comparison of Nusselt number prediction using Eq. (4) and the Nusselt number correlation from Stimpson et al. [2].

prediction of Eq. (4), the maximum error of 39% gets reduced to a maximum absolute error of 25% when using the predicted friction factor and 24% when using the experimental friction factor. The cause for the outlier is because the friction factor of the 1-mm channel from Wildgoose et al. [23] exhibited one of the highest friction factor values, while the Nusselt number was significantly lower compared to the rest of the samples evaluated. It is important to note that Eq. (4) was created using a total of 41 coupons, while the Stimpson et al. [2] correlation was created using a total of 10 coupons.

Similar to the Gnielinski correlation, Eq. (4) should only be used in turbulent flows when the Reynolds number is greater than 2300. Since air was the only fluid used to make Eq. (4), fluids where $Pr \approx 0.7$ should only be used. As a result of the datasets used to make Eq. (4), only curved channel shapes such as teardrop and circular designs should be used for the correlation.

A comparison of the same samples from Fig. 12 is shown in Fig. 14 for the prediction of Nusselt number using Stimpson et al. [2] and Eq. (4). Equation (4) is more effective at predicting Nusselt number when using the experimental friction factor and predicted friction factor from Eq. (3) compared to the correlation from Stimpson et al. [2] for the samples in Fig. 14. A noncircular channel shape (a pentagon) from Wildgoose et al. [24] is also included in Fig. 12. The maximum absolute error of the pentagon is 22% when using the experimental friction factor data and 5% when using the friction factor predicted from Eq. (3). Despite a higher error when predicting friction factor using Eq. (3) for pentagon, the Nusselt number correlation (Eq. (4)) exhibits a lower error.

Conclusion

Multiple circular and teardrop cooling channel coupons were fabricated over a range of different build considerations (build directions, radial build locations, and channel diameters) using a four-laser DMLS machine. Each of the 27 coupons was CT scanned to evaluate their geometric dimensions and internal surface roughness. Pressure loss and heat transfer of the coupons were measured over a range of fully turbulent Reynolds numbers.

For the samples presented in this paper, the hydraulic diameter did not change with radial build location. Channels with teardrop corrections at the 0-deg build direction contained hydraulic diameters lower than their design intent, while teardrop channels at the 45-deg and circular channels at the 90-deg build directions had hydraulic diameters higher than their design intent.

Surface roughness, specifically the arithmetic mean roughness, decreased as the build direction increased from 0 deg to 90 deg. Similar to hydraulic diameter, surface roughness was not a function of build location. The arithmetic mean roughness normalized by hydraulic diameter decreases as the build direction increases from 0 deg to 90 deg, regardless of diameter or radial build location.

In contrast to the arithmetic mean roughness-to-diameter ratio, the samples at the 90-deg build direction contained the highest friction factor relative to the 45-deg and 0-deg orientations for any given diameter. As the diameter decreased from 1.4 mm to 0.8 mm, the friction factor increased by more than two-thirds. Nusselt number followed different trends in build direction compared to the trends of friction factor and surface roughness. Despite the 90-deg samples exhibiting the highest friction factor, their Nusselt number was equal or lower compared to their 45-deg and 0-deg counterparts.

Several correlations from open literature for friction factor and Nusselt number were compared with the coupons from the current study and datasets in the literature. A density parameter using area ratios of the roughness elements and a correlation length parameter from an autocorrelation function applied to the surface struggled to correlate sandgrain roughness. Bulk roughness correlations from the literature, such as those using arithmetic mean roughness, were unsuccessful in correlating friction factor since samples can contain the same arithmetic mean roughness-to-diameter ratio but exhibit different friction factor values. By using a combination of roughness statistics, specifically the root mean square roughness and skewness, a correlation was developed that was able to reduce the error in predicting friction factor by half compared to additive-specific roughness correlations in the literature. Quantitatively, the presented friction factor correlation was able to predict samples within a maximum absolute error of 25% with an average absolute error of 12%.

A Nusselt number correlation was also created using the datasets for the friction factor correlation. The Nusselt number correlation was able to reduce the average error by half compared to additive-specific Nusselt correlations found in the literature. In more detail, the presented Nusselt number correlation was able to predict samples within a maximum absolute error of 39%, with an average absolute error of 8%.

In summary, friction factor and Nusselt number can be predicted using roughness statistics that are commonly quoted in AM part qualification. The correlations can be used for circular and teardrop channel shapes regardless of changes to machine, material, build direction, build location, and channel size.

Acknowledgment

Conflict of Interest

There are no conflicts of interest.

Data Availability Statement

The authors attest that all data for this study are included in the paper.

Nomenclature

f = Darcy friction factor, $f = \Delta P \dfrac{D_h}{L} \dfrac{2}{\rho u_{mean}^2}$

h = convective heat transfer coefficient, $h = \dfrac{Q_{in,heater} - \sum Q_{loss}}{A \cdot \Delta T_{lm}}$

k = thermal conductivity

p = channel perimeter

A = surface area

L = channel length

P = static pressure

S = channel pitch distance

T = temperature

k_s = sand grain roughness

z_{max} = maximum roughness height

z_{min} = minimum roughness height

z_{ref} = reference surface plane

z_{surf} = roughness height

A_c = cross-sectional flow area

A_f = frontal projected area

A_w = wetted frontal area

D_h = hydraulic diameter, $4A_c/p$

Q_{air} Q_{air} = $\dot{m}C_p(T_{out} - T_{in})$

Q_{heat} = energy from heaters

R_a = arithmetic mean roughness, $R_a = \dfrac{1}{n}\sum_{i=1}^{n} |z_{surf} - z_{ref}|$

R_{ku} = kurtosis, $R_{ku} = \dfrac{1}{nR_q^4}\sum_{i=1}^{n}(z_{surf} - z_{ref})^4$

R_q = root mean square roughness, $R_q = \sqrt{\dfrac{1}{n}\sum_{i=1}^{n}(z_{surf} - z_{ref})^2}$

R_{sk} = skewness, $R_{sk} = \dfrac{1}{nR_q^3}\sum_{i=1}^{n}(z_{surf} - z_{ref})^3$

R_z = mean roughness depth, $R_z = \dfrac{1}{5}\sum_{i=1}^{5}(z_{max} - z_{min})_i$

T_{LM} = log-mean temperature, $\Delta T_{LM} = \dfrac{(\Delta T_{in} - \Delta T_{out})}{\ln\left(\frac{T_s - T_{in}}{T_s - T_{out}}\right)}$

Nu = Nusselt number, hD_h/k_{air}

Pr = Prandtl number

Re = Reynolds number, $u_{mean} D_h/\nu$

Greek Symbols

λ = correlation length

ν = kinematic viscosity

ρ = fluid density

Λ_s = Sigal and Danberg density parameter

Subscripts

des = design intent dimension

exp = value measured from experiments

in = inlet condition

meas = measured dimension from CT Scan

out = exit condition

pred = value predicted from a correlation

s = surface condition

References

[1] Ventola, L., Robotti, F., Dialameh, M., Calignano, F., Manfredi, D., Chiavazzo, E., and Asinari, P., 2014, "Rough Surfaces With Enhanced Heat Transfer for Electronics Cooling by Direct Metal Laser Sintering," Int. J. Heat Mass Transfer, 75, pp. 58–74.

[2] Stimpson, C. K., Snyder, J. C., Thole, K. A., and Mongillo, D., 2016, "Scaling Roughness Effects on Pressure Loss and Heat Transfer of Additively Manufactured Channels," ASME J. Turbomach., 139(2), p. 021003.

[3] Snyder, J. C., Stimpson, C. K., Thole, K. A., and Mongillo, D. J., 2015, "Build Direction Effects on Microchannel Tolerance and Surface Roughness," ASME J. Mech. Des., 137(11), p. 111411.

[4] Snyder, J. C., and Thole, K. A., 2020, "Tailoring Surface Roughness Using Additive Manufacturing to Improve Internal Cooling," ASME J. Turbomach., 142(7), p. 071004.

[5] Yeung, H., Lane, B., and Fox, J., 2019, "Part Geometry and Conduction-Based Laser Power Control for Powder Bed Fusion Additive Manufacturing," Addit. Manuf., 30, p. 100844.

[6] Kleszczynski, S., Ladewig, A., Friedberger, K., zur Jacobsmuhlen, J., Merhof, D., and Witt, G., 2015, "Position Dependency of Surface Roughness in Parts From Laser Beam," Proceedings of the 2015 International Solid Freeform Fabrication Symposium, Austin, TX, Aug. 10–12, pp. 360–370.

[7] Subramanian, R., Rule, D., and Nazik, O., 2021, "Dependence of LPBF Surface Roughness on Laser Incidence Angle and Component Build Orientation," ASME Turbo Expo 2021: Turbomachinery Technical Conference and Exposition, Virtual, Online.

[8] Wang, P., Yang, M., Wang, Z., and Zhang, Y., 2014, "A New Heat Transfer Correlation for Turbulent Flow of Air With Variable Properties in Noncircular Ducts," ASME J. Heat Transfer, 136(10), p. 101701.

[9] Snyder, J. C., and Thole, K. A., 2020, "Effect of Additive Manufacturing Process Parameters on Turbine Cooling," ASME J. Turbomach., 142(5), p. 051007.

[10] Kandlikar, S. G., Schmitt, D., Carrano, A. L., and Taylor, J. B., 2005, "Characterization of Surface Roughness Effects on Pressure Drop in Single-Phase Flow in Minichannels," Phys. Fluids, 17(10), p. 100606.

[11] Nikuradse, J., 1950, "Laws of Flow in Rough Pipes," J. Appl. Phys., 3(Nov.), p. 399.

[12] Mazzei, L., Da Soghe, R., and Bianchini, C., 2022, "Calibration of a CFD Methodology for the Simulation of Additively Manufactured Components Accounting for the Effects of Diameter and Printing Direction on Friction and Heat Transfer," ASME J. Turbomach., 144(8).

[13] Thole, K. A., Lynch, S., and Wildgoose, A. J., 2021, "Review of Advances in Convective Heat Transfer Developed Through Additive Manufacturing," Adv. Heat Transfer, 53, pp. 249–325.

[14] Zhou, L., Zhu, Y., Liu, H., He, T., Zhang, C., and Yang, H., 2021, "A Comprehensive Model to Predict Friction Factors of Fluid Channels Fabricated Using Laser Powder Bed Fusion Additive Manufacturing," Addit. Manuf., 47, p. 102212.

[15] Goodhand, M. N., Walton, K., Blunt, L., Lung, H. W., Miller, R. J., and Marsden, R., 2016, "The Limitations of Using 'Ra' to Describe Surface Roughness," ASME J. Turbomach., 138(10), p. 101003.

[16] Van Rij, J. A., Belnap, B. J., and Ligrani, P. M., 2002, "Analysis and Experiments on Three-Dimensional, Irregular Surface Roughness," ASME J. Fluids Eng., 124(3), pp. 671–677.

[17] Forooghi, P., Stroh, A., Magagnato, F., Jakirlić, S., and Frohnapfel, B., 2017, "Toward a Universal Roughness Correlation," ASME J. Fluids Eng., 139(12), p. 121201.

[18] Flack, K. A., and Schultz, M. P., 2010, "Review of Hydraulic Roughness Scales in the Fully Rough Regime," ASME J. Fluids Eng., 132(4), p. 041203.

[19] Sigal, A., and Danberg, J. E., 1990, "New Correlation of Roughness Density Effect on the Turbulent Boundary Layer," AIAA J., 28(3), pp. 554–556.

[20] Stimpson, C. K., Snyder, J. C., Thole, K. A., and Mongillo, D., 2016, "Roughness Effects on Flow and Heat Transfer for Additively Manufactured Channels," ASME J. Turbomach., 138(5), p. 051008.

[21] Mazzei, L., Da Soghe, R., and Bianchini, C., 2022, "Calibration of a Computational Fluid Dynamics Methodology for the Simulation of Roughness Effects on Friction and Heat Transfer in Additive Manufactured Components," ASME J. Turbomach., 144(8), p. 081002.

[22] Snyder, J. C., Stimpson, C. K., Thole, K. A., and Mongillo, D., 2016, "Build Direction Effects on Additively Manufactured Channels," ASME J. Turbomach., 138(5), p. 051006.

[23] Wildgoose, A. J., Thole, K. A., Sanders, P., and Wang, L., 2021, "Impact of Additive Manufacturing on Internal Cooling Channels With Varying Diameters and Build Directions," ASME J. Turbomach., 143(7), p. 071003.

[24] Wildgoose, A. J., and Thole, K. A., 2023, "Heat Transfer and Pressure Loss of Additively Manufactured Internal Cooling Channels With Various Shapes," ASME J. Turbomach., 145(7), p. 071011.

[25] Wildgoose, A. J., Thole, K. A., Subramanian, R., Kerating, L., and Kulkarni, A., 2023, "Impacts of the Additive Manufacturing Process on the Roughness of Engine Scale Vanes and Cooling Channels," ASME J. Turbomach., 145(4), p. 041013.

[26] Kamat, A. M., and Pei, Y., 2019, "An Analytical Method to Predict and Compensate for Residual Stress-Induced Deformation in Overhanging Regions of Internal Channels Fabricated Using Powder Bed Fusion," Addit. Manuf., 29, p. 100796.

[27] Segersäll, M., 2013, Nickel-Based Single-Crystal Superalloys—The Crystal Orientation Influence on High Temperature Properties, Vol. 1568, Linköping Studies in Science and Technology Licentiate Thesis.

[28] Volume Graphics, 2021, VGStudio MAX.

[29] Reinhart, C., 2011, Industrial CT & Precision, Volume Graphics GmbH, Heidelberg, Germany.

[30] Wildgoose, A. J., and Thole, K. A., 2022, "Variability in Additively Manufactured Turbine Cooling Features," J. Glob. Power Propuls. Soc.

[31] Klingaa, C. G., Bjerre, M. K., Baier, S., De Chiffre, L., Mohanty, S., and Hattel, J. H., 2019, "Roughness Investigation of SLM Manufactured Conformal Cooling Channels Using X-Ray Computed Tomography," Proceedings of the 9th Conference on Industrial Computer Tomography, Padova, Italy, Feb. 13–15.

[32] Munson, R., Young, B., and Okiishi, D. F., and H, T., 1990, Fundamentals of Fluid Mechanics, Wiley & Sons, Hoboken, NJ.

[33] Figliola, R. S., and Beasley, D. E., 2005, Theory and Design for Mechanical Measurments, Wiley & Sons, Hoboken, NJ.

[34] Molitor, V. D., 2018, Experimental Study on Pressure Losses in Additive Manufactured Channels, RWTH, Aachen.

[35] Nambisan, J., 2020, "Experimental Study on Pressure Losses in Additively Manufactured and Machined Orifices," Master's Thesis, Linköping University, Linköping, Sweden.